Exploring the Application of Hexagonal SnS$_2$ Nanoplates Covered with a 3D Graphene Network for Lithium Sulfur Batteries

Baohai Liu, Wenxu Wang, Honglei Li, Zhixu Jian, Yalan Xing, Shichao Zhang[*]

School of Materials Science and Engineering, Beihang University, Beijing 100191, PR China
[*]E-mail: csc@buaa.edu.cn

With its high specific capacity, the lithium sulfur battery is seen by many as the battery of the future. However, the Li–S battery still faces a host of problems, mainly connected to its poor cycling performance due to the "shuttle effect". As they show strong chemical absorption and are reaction sites to polysulfide species, sulfiphilic hosts are used in cathode material. For this paper, tin sulfide (SnS$_2$) nanoplates were incorporated with a 3D graphene network using a simple hydrothermal method and a reduction process. After the infiltration of sulfur, the S/rGO-SnS$_2$ exhibited a high initial discharge capacity of 1150.1 mAh g^{-1} and excellent stability after 100 cycles (844.6 mAh g^{-1}). The superior stability and reversibility is due to the synergy between the high-active sulfiphilic SnS$_2$ and high-conductivity 3D graphene network. This result shows a potential approach to the application of Li–S batteries.

1. INTRODUCTION

The increasing demand for energy storage systems has stimulated the rapid development of battery technology. Over the past decade, lithium-ion batteries have been widely used in portable electronic devices and electric vehicles, but their future will be problematic without further improvement of their higher energy density and a longer useful life. The lithium sulfur battery, a promising candidate for future battery systems, exhibits a high specific capacity of 1675 mAh g^{-1} and energy density of 2600 Wh kg^{-1} [1,2]. In addition, the natural abundance of sulfur elements can reduce costs, suggesting the lithium sulfur battery is a superior replacement for today's batteries [3].

Although countless efforts have been made to accelerate the implementation of lithium sulfur batteries, a number of drawbacks are still blocking progress [4]. The first issue is related to the

electrically insulating nature of sulfur and its reduced product, lithium sulfide, as this affects the rate performance of the batteries [5]. The second issue concerns the high solubility of the polysulfide intermediates in the electrolyte during the cycling process, specifically the long chain polysulfide (Li_2S_8 to Li_2S_4), which is the main reason the batteries lose capacity [6,7]. The third issue is related to the large volume change during the charge/discharge process, which results in the structural destruction of the electrode material [8].

To solve these issues, carbonaceous materials are frequently chosen as a host for the sulfur, on account of their enhanced conductivity and the physical capsulation capacity of polysulfide species. These carbonaceous materials include 1D carbon nanotubes [9,10], 2D graphene [11,12], micro/mesoporous carbon [13,14], and hollow carbon spheres [15,16]. However, due to non-polar C-C bonding, the interaction between the polar polysulfide and carbon is inherently weak [17]. As a result, the dissolution of polysulfide is still inevitable when a carbon host material is used. Another attractive approach beyond physical confinement is to use inorganic polar host materials [18], generally metal oxides, nitrides, and sulfides, because they have a stronger chemical affinity with polysulfide species. In other research, different inorganic materials, such as $Mg_{0.6}Ni_{0.4}O$ [19], TiO_2 [20], MnO_2 [21], VN [22], CoS_2 [23] and Al_2O_3 [24], have been found to improve cycling performance when used as cathode host material in lithium sulfur batteries. Recent studies have shown that tin sulfide (SnS_2) exhibits a promising trapping effect with polysulfide species [25]. However, the intrinsic low electric conductivity of SnS_2 restricts its further application as a host material for lithium sulfur batteries [26].

For this paper, hexagonal SnS_2 nanoplates covered with a graphene composite were prepared using a simple hydrothermal method followed by a reduction process. The resulting composite was further applied as an effective polysulfide immobilizer for the preparation of the sulfur cathode. It is noteworthy that the hexagonal SnS_2 nanoplates provided more active sites to anchor the polysulfide, and that the graphene proved an effective network for rapid electronic transfer.

2. EXPERIMENTAL SECTION

2.1. Materials synthesis

The synthesis of the $S/rGO-SnS_2$ is illustrated in Fig. 1. The process of preparation was similar to a previous report with only a slight modification [27]. Typically, 50 mg of graphite oxide (modified Hummers' method) was added to 30 mL deionized water under ultrasonication for 1 h. Then, 0.5 mmol tin (IV) chloride pentahydrate ($SnCl_4·5H_2O$) was dissolved in the dispersion with magnetic stirring for 1 h, with 1 mmol thiourea (NH_2CSNH_2) then added to the above dispersion with magnetic stirring for another 1 h. After that, the mixture was transferred into a Teflon-lined stainless-steel autoclave and hydrothermally treated at 160 °C for 15 h. The $GO-SnS_2$ sample obtained was separated by centrifugation and dried in a vacuum oven at 60 °C overnight. The sample was then dispersed in deionized water with an addition of 0.3 g l-ascorbic acid and then heated to 95 °C in a water bath for 3 h. Finally, the $rGO-SnS_2$ was obtained by collecting the solid resultant with a careful wash. For the synthesis of $S/rGO-SnS_2$ composite, $rGO-SnS_2$ sample and sublimed sulfur were thoroughly mixed at a

weight ratio of 3:7 and sealed in a glass tube container with argon gas. The container was then heated in an oven at 155 °C for 24 h to obtain the product.
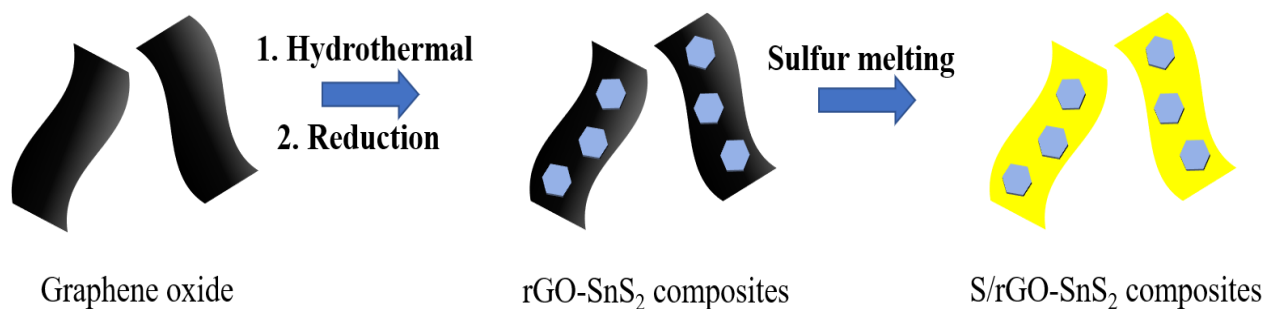
Figure 1. Schematic of the preparation of S/rGO-SnS$_2$ composite

2.2. Characterization

Field-emission scanning electron microscopy (Hitachi S-4800), transmission electron microscopy (JEM-2100F), and high-resolution transmission electron microscopy (FEI, Tecnai G2 F20) were used to characterize the morphology and microstructure of the as-prepared samples. The atomic information of the samples was also investigated using an energy dispersive X-ray spectrometer (EDS) which was attached to SEM. X-ray diffraction (XRD, Rigaku D/Max-2400) was conducted from 10° to 80° at a scan rate of 0.5° min^{-1} to analyze the crystal structures of the samples. Thermal gravimetric analysis (TGA) was carried out on a thermogravimetric analyzer (STA-449C, NETZSCH) at a heating rate of 10 °C min^{-1} from room temperature to 500 °C in an Argon atmosphere.

2.3. Electrochemical measurement

The electrode material for the test was prepared by mixing 70 wt.% as-prepared samples, 20 wt.% conducting acetylene black, and 10 wt.% PVDF binder in a N-meth4yl-2-pyrrolidinone (NMP) solvent to form a uniform slurry. The slurry was then coated onto aluminum foil and dried in a vacuum at 60 °C for 12h to evaporate the solvent completely. The working electrodes were finally obtained by cutting the coated foil into discs. The active material loading on each electrode was 0.8–1.0 mg. Cells (CR2032) were assembled in an Ar atmosphere glove box with lithium foil as both reference and counter electrode. A Celgard 2400 membrane was used as separator and a mixed solution of DOL and DME (1:1 by volume) was used as electrolyte. The cells were galvanostatically charged/discharged on a NWEARE BTS-610 instrument in the range of 1.7–2.8 V versus Li$^+$/Li. Cyclic Voltammetry (CV) was carried out on a CHI 660D electrochemical workstation between 2.8 V and 1.7 V at a scan rate of 0.1 mV s^{-1}. Electrochemical impedance spectroscopy (EIS) was measured in the frequency range from 100 kHz to 0.01 Hz on a Zahner IM6e electrochemical workstation.

3. RESULTS AND DISCUSSION

As shown in Figure 1, the preparation of rGO-SnS$_2$ used the hydrothermal method followed by chemical reduction. During the process of mixture, Sn^{4+} ions were first absorbed by the hydroxyl, carboxyl, and epoxy groups, these being the abundant functional groups of GO [28]. Then H$_2$S was released by decomposing thiourea during the hydrothermal treatment, which served as a sulfur provider to form SnS$_2$ nuclei. Finally, it was further reduced by l-ascorbic at a mild temperature compared with other reducing agents [29]. Due to the presence of graphene, SnS$_2$ grew on the surface, in close contact with GO sheets. This structure ensured an effective electron transfer rate and yielded a sufficient surface area to anchor the polysulfide.
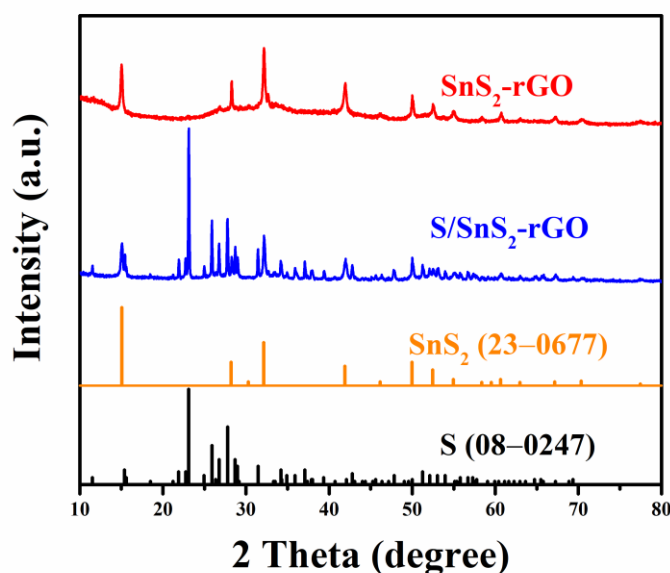
Figure 2. The XRD pattern of the as-prepared rGO-SnS$_2$ and S/rGO-SnS$_2$

The XRD patterns of the rGO-SnS$_2$ and S/rGO-SnS$_2$ are presented in Figure 2. The diffraction pattern of rGO-SnS$_2$ shows several peaks at 15.0, 28.3, 32.1, 41.9, 50.1, 52.5, and 55.1°, corresponding to the (0 0 1), (1 0 0), (1 0 1), (1 0 2), (1 1 0), (1 1 1), and (1 0 3) crystal planes of SnS$_2$ (JCPDS 23-0677), respectively [30]. It also indicates a weak peak with 2θ valve at around 26.1°, which originates in the (002) plane of graphene nanosheets [29]. No other impurity peak was observed. Additionally, the intensity of the peak at 2θ = 15.0° was evidently decreased in comparison to the PDF card, indicating that the growth of the crystal plane (001) was hampered due to the presence of graphene [31]. This result also closely agrees with the SEM and TEM images, showing that the SnS$_2$ has a special hexagonal nanoplate structure. However, in the XRD pattern of S/rGO-SnS$_2$, the peaks of SnS$_2$ could still be clearly observed, while the newly-presented peaks could well be indexed to orthorhombic sulfur. This result confirms the noteworthy infiltration of sulfur in rGO-SnS$_2$.
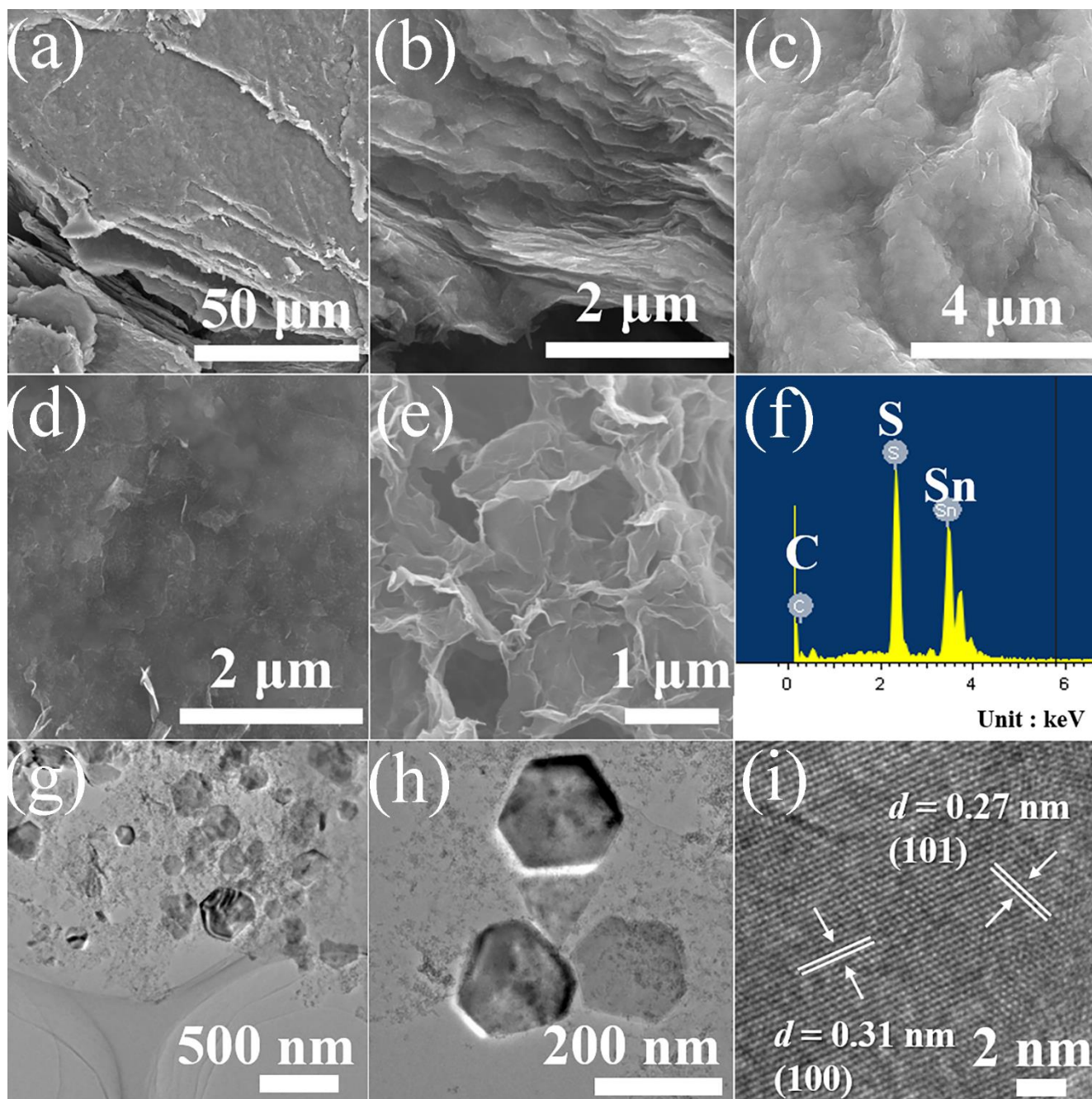
Figure 3. Micro structures of rGO-SnS$_2$: SEM image (a) at low magnification, (b) of side face, (c)(d) of front side at high magnification, (e) pure graphene; (f) EDS results; TEM images (g) at low magnification, (h) at high magnification; (i) HRTEM image

The morphologies of as-prepared rGO-SnS$_2$ were investigated by SEM; the results are as shown in Figure 3. The sandwich-like layered graphene can be seen, at low magnification, in Fig. 3a. Compared with pure graphene, the surface of the sample is rough (Fig. 3e), suggesting the existence of SnS$_2$. Fig. 3b shows, at high magnification, the side face of the graphene, clearly presenting the layered structure of rGO-SnS$_2$. Fig. 3c and Fig. 3d show the front side of the sample in different areas at higher magnification. Both present small SnS$_2$ particles, covering the graphene. This sandwich-like layered structure provides sufficient volume for sulfur infiltration and the construction of a three-dimensional

conductive framework, implying great potential for effective Li–S battery host material. Fig. 3f shows the EDS result collected on the area in Fig. 3g, and further confirms the existence of Sn, S and C. The element O was not detected, verifying the success of the deoxidation of graphene oxide. Transmission electron microscopy (TEM) analysis was used to detect the microstructure of rGO-SnS$_2$ composite. As presented in Fig. 3f, the SnS$_2$ nanoplates are well-distributed on the thin graphene sheet. In addition, the rGO-SnS$_2$ composite possesses a face-to-face structure which strengthens the contact between the SnS$_2$ nanoplates and the graphene. Most of the hexagonal SnS$_2$ nanoplates have an average diameter of ~150 nm, as shown in Figure 3h, an enlarged TEM image. HRTEM was also employed to characterize nanocrystal in Fig. 3i; the lattice fringes of SnS$_2$ display interplanar spacings of 0.31 and 0.27 nm, which are consistent with those of the (100) and (101) planes of SnS$_2$, respectively [32]. The result also closely corresponds with the above XRD results.
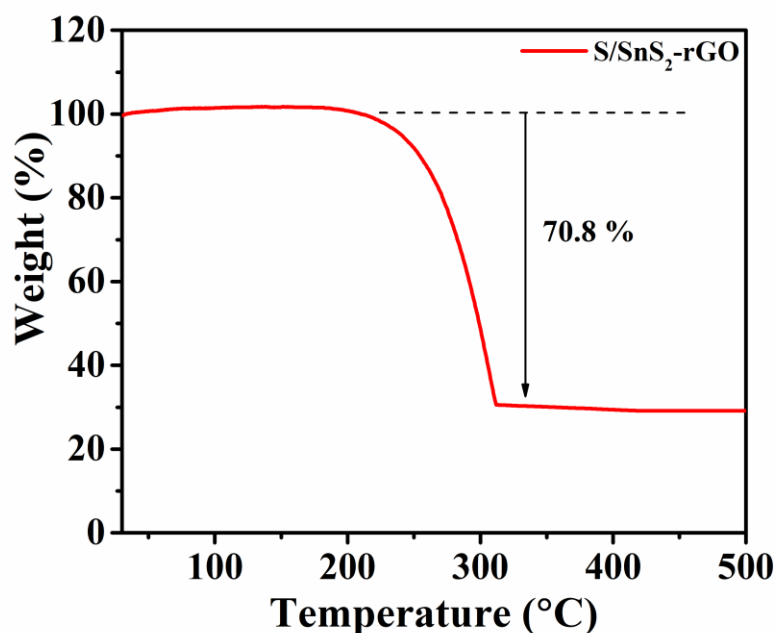

Figure 4. The weight loss curve of S/rGO-SnS$_2$ composite by TGA

A thermogravimetry analysis (TGA) of the S/rGO-SnS$_2$ composite was taken to determine the sulfur content. As the curve in Figure 4 shows, major weight loss appears in the temperature range of 200 to 350°C. This weight loss can be attributed to the sublimation of sulfur in the composite [11]. The sulfur content was measured to be 70.8 wt%.

The electrochemical performances of the as-prepared S/rGO-SnS$_2$ composite were investigated with respect to its use as a possible cathode for Li–S batteries; the results are shown in Figure 5. Cyclic voltammetry (CV) tests were conducted under a voltage window of 1.7–2.8 V vs. Li/Li$^+$ at a scan rate of 0.1 mV s^{-1}. The results are presented in Fig. 5a. Two typical cathodic peaks can be clearly observed. The higher peak at ~2.2 V corresponds to the reduction process from S$_8$ molecule to long-chain intermediate polysulfides (Li$_2$S$_x$, 4≤x≤8). The lower peak at ~1.95 V represents the following

reduction to the final product Li_2S. The continuous anodic peaks are located at 2.4–2.5 V, which corresponds to the reverse oxidization reaction from Li_2S to elemental sulfur [33].
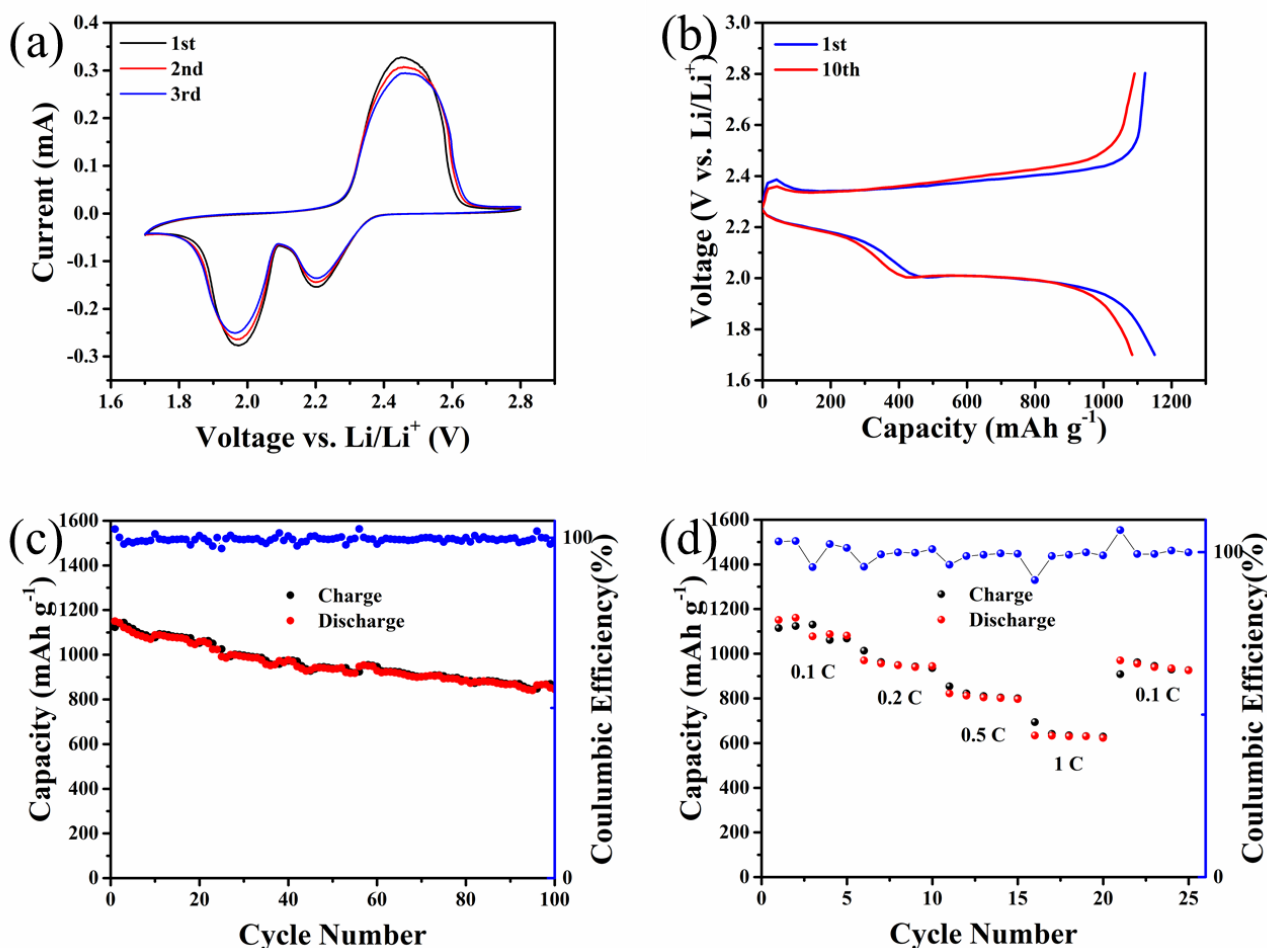
Figure 5. The electrochemical performance of Li–S batteries with S/rGO-SnS$_2$ cathode: (a) CV curves between 1.7–2.8 V; (b) charge/discharge profiles; (c) cycling performances at 0.2C; (d) rate performances.

Moreover, during the first three cycles in the CV test, all the cathodic and anodic peaks overlapped quite well, confirming the superior stability performance of the S/rGO-SnS$_2$ electrode. Fig. 5b shows the charge/discharge voltage profiles of S/rGO-SnS$_2$ at 1st cycle and 10th cycle between 1.7 and 2.8 V. Two typical plateaus (about 2.2 and 2.0 V) can be observed at both the 1st cycle and the 10th cycles, agreeing well with the two cathodic peaks in the CV analysis. The decay of capacity is not obvious, suggesting a good capacity retention. The cycling performance of S/rGO-SnS$_2$ cathode was tested at 0.2 C in Fig. 5c. The S/rGO-SnS$_2$ cathode delivers a specific capacity of 1150.1 mAh g^{-1} at first cycle, and remains at 844.6 mAh g^{-1} after 100 cycles, showing a great cycling stability. Furthermore, the average capacity decay is 0.31% per cycle, indicating a good cycling performance. In addition, the coulombic efficiency during the cycling test remained stable above 98%, which also implies the superior stability of the electrode. This superior stability can be attributed to the anchor effect of sulfiphilic SnS$_2$: in other words, the polar host SnS$_2$ has a strong affinity with polysulfide

species, with the result that its dissolution is reduced in the electrolyte and prevents a severe shuttle effect [23,34,35]. The comparison results of cycling performance between the S/rGO-SnS$_2$ cathode and other similar Li-S cathodes are presented in Table 1. Even with the highest sulfur content among these cathode materials, the initial capacity and retention after cycling are still remarkable for S/rGO-SnS$_2$, proving its outstanding cycling performance. Furthermore, as shown in Fig. 5d, the rate performance of S/rGO-SnS$_2$ electrode, after testing at different current rates of 0.1 C, 0.2 C, 0.5 C and 1 C, delivers specific capacities of 1150.8, 969.6, 821.9, and 633.9 mAh g^{-1}. More importantly, with the return of current density to the initial value of 0.1 C, discharge capacity still regains 970 mAh g^{-1}. From the fact of the high maintenance of specific capacity after cycling at high rate, it can be concluded that S/rGO-SnS$_2$ has excellent reversibility and reliability at various rates.

Table 1. Performances comparison of S/rGO-SnS$_2$ with some other similar Li – S cathode materials

	Sulfur content	Initial capacity (mAh g^{-1})	Retention	Ref.
S/rGO-SnS$_2$	70.8 wt%	1150.1 at 0.2 C	73.4% after 100 cycles	This work
rGO@Sulfur Spheres	68.8 wt%	827 at 0.2 C	46.9% after 100 cycles	[36]
Self-supporting porous CoS$_2$/rGO-S	60 wt%	993.5 at 0.5 C	74.4% after 110 cycles	[37]
PEO-Linked MoS$_2$– Graphene-S	62 wt%	1231 at 0.2 C	72.7% after 100 cycles	[38]
SnS$_2$-Anchored Sulfur-Hollow Carbon Nanospheres	64.2 wt%	1237.5 at 0.2 C	74.7% after 200 cycles	[26]
Flexible Carbon Nanotube– Graphene/Sulfur	53 wt%	911.5 at 0.2 C	84.7% after 100 cycles	[39]

On the basis of above results, the superior electrochemical performance of S/rGO-SnS$_2$ is confirmed. The reasons for this superior performance are as follows. First, rGO-SnS$_2$ possesses a 3D-connected network structure consisting of layered graphene, which, compared with sole SnS$_2$, is beneficial to mass transport and superior electron conductivity. Secondly, the existence of SnS$_2$ on the surface helps to anchor the polysulfide species and to suppress the shuttle effect by chemical absorptivity. Graphene has only non-polar C-C chemical bonds internally, therefore the incorporation of polar SnS$_2$ would greatly improve the capacity of the whole cathode to slow the rate of capacity loss. Thirdly, this structure can withstand great volume expansion of active material during the cycling process. As a result, the S/rGO-SnS$_2$ cathode displays notable cycling performance and remarkable reversibility.

4. CONCLUSION

In summary, the rGO-SnS$_2$ composite was successfully synthesized via a hydrothermal method following by a reduction process. The composite was stacked by layered graphene in a 3D-connected structure. The hexagonal SnS$_2$ nanoplate was evenly covered over the surface of the graphene. This structure provides a stable and sufficient space for sulfur infiltration and a conductive network. As a result, S/rGO-SnS$_2$ delivers a high initial specific capacity of 1150.1 mAh g^{-1} and remains at 844.6 mAh g^{-1} after 100 cycles as a cathode for Li-S batteries. This work verifies the synergy between application of sulfiphilic SnS$_2$ and a 3D conductive graphene network, which suggests a promising orientation for the energy storage domain.

References

1. H.-J. Peng, J.-Q. Huang, X.-B. Cheng and Q. Zhang, *Adv. Energy Mater.,* 7 (2017) 1700260.
2. Z. W. Seh, Y. Sun, Q. Zhang and Y. Cui, *Chemical Society reviews,* 45 (2016) 5605.
3. A. Manthiram, Y. Fu, S.-H. Chung, C. Zu and Y.-S. Su, *Chemical reviews,* 114 (2014) 11751.
4. M. Liu, D. Zhou, Y.-B. He, Y. Fu, X. Qin, C. Miao, H. Du, B. Li, Q.-H. Yang, Z. Lin, T. S. Zhao and F. Kang, *Nano Energy,* 22 (2016) 278.
5. Y. Cui, M. Wu, C. Scott, J. Xie and Y. Fu, *RSC Adv.,* 6 (2016) 52642.
6. Q. Pang, X. Liang, C. Y. Kwok, J. Kulisch and L. F. Nazar, *Adv. Energy Mater.,* 7 (2017) 1601630.
7. B. Yan, X. Li, Z. Bai, X. Song, D. Xiong, M. Zhao, D. Li and S. Lu, *Journal of Power Sources,* 338 (2017) 34.
8. Z. Zhang, L.-L. Kong, S. Liu, G.-R. Li and X.-P. Gao, *Adv. Energy Mater.,* 7 (2017) 1602543.
9. M. Li, R. Carter, A. Douglas, L. Oakes and C. L. Pint, *ACS nano,* 11 (2017) 4877.
10. Y. Mao, G. Li, Y. Guo, Z. Li, C. Liang, X. Peng and Z. Lin, *Nature communications,* 8 (2017) 14628.
11. B. Li, S. Li, J. Liu, B. Wang and S. Yang, *Nano letters,* 15 (2015) 3073.
12. S. Lu, Y. Chen, X. Wu, Z. Wang and Y. Li, *Scientific reports,* 4 (2014) 4629.
13. Z. Li, L. Yuan, Z. Yi, Y. Sun, Y. Liu, Y. Jiang, Y. Shen, Y. Xin, Z. Zhang and Y. Huang, *Adv. Energy Mater.,* 4 (2014) 1301473.
14. H.-J. Peng, J.-Q. Huang, M.-Q. Zhao, Q. Zhang, X.-B. Cheng, X.-Y. Liu, W.-Z. Qian and F. Wei, *Adv. Funct. Mater.,* 24 (2014) 2772.
15. J. Zang, T. An, Y. Dong, X. Fang, M. Zheng, Q. Dong and N. Zheng, *Nano Res.,* 8 (2015) 2663.
16. Q. Sun, B. He, X.-Q. Zhang and A.-H. Lu, *ACS nano,* 9 (2015) 8504.
17. H. Shi, W. Lv, C. Zhang, D.-W. Wang, G. Ling, Y. He, F. Kang and Q.-H. Yang, *Adv. Funct. Mater.,* 28 (2018) 1800508.
18. Q. Pang, D. Kundu, M. Cuisinier and L. F. Nazar, *Nature communications,* 5 (2014) 4759.
19. H. Tang, S. Yao, M. Jing, X. Wu, J. Hou, X. Qian, D. Rao, X. Shen, X. Xi and K. Xiao, *Journal of Alloys and Compounds,* 650 (2015) 351.
20. Z. Wei Seh, W. Li, J. J. Cha, G. Zheng, Y. Yang, M. T. McDowell, P.-C. Hsu and Y. Cui, *Nature communications,* 4 (2013) 1331.
21. X. Liang and L. F. Nazar, *ACS nano,* 10 (2016) 4192.

22. Z. Sun, J. Zhang, L. Yin, G. Hu, R. Fang, H.-M. Cheng and F. Li, *Nature communications,* 8 (2017) 14627.
23. Z. Yuan, H.-J. Peng, T.-Z. Hou, J.-Q. Huang, C.-M. Chen, D.-W. Wang, X.-B. Cheng, F. Wei and Q. Zhang, *Nano letters,* 16 (2016) 519.
24. Z. Zhang, Y. Lai, Z. Zhang, K. Zhang and J. Li, *Electrochimica Acta,* 129 (2014) 55.
25. X. Li, Y. Lu, Z. Hou, W. Zhang, Y. Zhu, Y. Qian and J. Liang, *ACS applied materials & interfaces,* 8 (2016) 19550.
26. X. Li, L. Chu, Y. Wang and L. Pan, *Materials Science and Engineering: B,* 205 (2016) 46.
27. J. Ye, L. Qi, B. Liu and C. Xu, *Journal of colloid and interface science,* 513 (2017) 188.
28. H. Wang, L.-F. Cui, Y. Yang, H. Sanchez Casalongue, J. T. Robinson, Y. Liang, Y. Cui and H. Dai, *Journal of the American Chemical Society,* 132 (2010) 13978.
29. J. Ye, Q. Hao, B. Liu, Y. Li and C. Xu, *Chemical Engineering Journal,* 315 (2017) 115.
30. H. Tang, X. Qi, W. Han, L. Ren, Y. Liu, X. Wang and J. Zhong, *Applied Surface Science,* 355 (2015) 7.
31. Y. Chang, J. Li, B. Wang, H. Luo, H. He, Q. Song and L. Zhi, *J. Mater. Chem. A,* 1 (2013) 14658.
32. Y. Zhang, P. Zhu, L. Huang, J. Xie, S. Zhang, G. Cao and X. Zhao, *Adv. Funct. Mater.,* 25 (2015) 481.
33. Y. An, Q. Zhu, L. Hu, S. Yu, Q. Zhao and B. Xu, *J. Mater. Chem. A,* 4 (2016) 15605.
34. M. Li, J. Zhou, J. Zhou, C. Guo, Y. Han, Y. Zhu, G. Wang and Y. Qian, *Materials Research Bulletin,* 96 (2017) 509.
35. G. Zhou, H. Tian, Y. Jin, X. Tao, B. Liu, R. Zhang, Z. W. Seh, D. Zhuo, Y. Liu, J. Sun, J. Zhao, C. Zu, D. S. Wu, Q. Zhang and Y. Cui, *Proceedings of the National Academy of Sciences of the United States of America,* 114 (2017) 840
36. F. Liu, J. Liang, C. Zhang, L. Yu, J. Zhao, C. Liu, Q. Lan, S. Chen, Y.-C. Cao and G. Zheng, *Results in Physics,* 7 (2017) 250.
37. X. Hong, S. Li, X. Tang, Z. Sun and F. Li, *Journal of Alloys and Compounds,* 749 (2018) 586.
38. X. Li, C. Yin, Z. Yue, L. Zhou, Y. Li and J. Shi, *ACS Sustainable Chem. Eng.,* 6 (2017) 974.
39. Y. Chen, S. Lu, X. Wu and J. Liu, *J. Phys. Chem. C,* 119 (2015) 10288.